Digital Object Identifier: 10.1016/j.solener.2024.113187

Source: https://www.sciencedirect.com/science/article/pii/S0038092X2400882X

Effective Intrinsic Charge Carrier Correction for Interface Charge Transfer Modeling of Perovskite Solar Cells in Dark Conditions ⋆

J. A. Jiménez-Tejada[a,*], M. García-Rosell[a], O. Almora[b], P. López-Varo[c]

[a]*Departamento de Electrónica y Tecnología de Computadores, CITIC-UGR, Universidad de Granada, Granada 18071, Spain*
[b]*Department of Electrical Electronic and Automatic Engineering, Universitat Rovira i Virgili, Tarragona 43007, Spain*
[c]*Institut Photovoltaïque d'Île-de-France 30 RD 128, 91120, Palaiseau, France*

Abstract

Modeling the transport at the interfaces between the charge-transport-layer (CTL) and the perovskite is essential to describe the performance of perovskite solar cells (PSCs), whose electrical response is driven by dual ionic and electronic transport. This ionic-electronic transport promotes peculiar capacitive behaviors, such as the case of dark current-voltage hysteresis experiments with strong dependency on the CTL. In this work, we develop a simulation model based on the drift-diffusion differential equations with a specific treatment of the interfaces. We model the perovskite/CTL (pvk/CTL) interface as a buffer region in which band-to-band or Shockley-Read-Hall (SRH) recombination take place. This buffer region has its own effective bandgap energy and layer thickness. Moreover, current leakages are incorporated in the simulation in order to achieve a similar order of magnitude to that measured in experimental current densities. Our model is tested with dark current-voltage experiments, and a similar trend is observed between the medium/high-frequency hysteresis in the experimental and simulated current-voltage curves. We highlight the importance of considering material modifications in interface recombination models for interpreting experimental hysteresis and to quantify the role of selective contacts in the electrical response of PSCs.

Keywords: Perovskite solar cells, modeling interfaces, hysteresis, drift-diffusion simulation

1. Introduction

Perovskite-solar cells (PSCs) exhibit a remarkable performance [1] due to the high values of the charge carrier mobility and diffusion length, light absorption coefficients [2], large defect tolerance [3] and tunable direct band gap. In addition, the use of solution-based and low-temperature fabrication processes allows for low-cost manufacturing. The impressive increase in photovoltaic performance, achieved from first reports [4] to recent values of efficiency (over 26%) [5, 6], has redirected research objectives onto getting devices with higher stability and larger area. However, although a great number of research results have been published on PSCs up to date, the understanding of the electrical response of these devices continues to be challenging.

The ionic-electronic phenomena of the metal halide perovskite (pvk) material family remains a puzzling subject [7]. It not only relates to the device performance stability [8], but also manifests in the hysteresis of the current density-voltage (*J-V*) curves [9], among others [10]. Accordingly, several research works have focused on understanding how ion migration and ion distribution throughout the perovskite affect the performance of PSCs [11, 12, 13, 14, 15, 16, 17], and more interestingly, their contribution to long-term instability [18, 19]. Notably, mobile ions accumulate towards the interfaces between the perovskite and the charge transport layers [20, 21, 16] increasing interface recombination and even activating chemical reactions between the perovskite material and the charge transport layers (CTLs) [22, 23].

Interestingly, the interface phenomena with halide perovskites can be critically dependent on the material properties towards the CTLs, where the effective bandgap energy *Eg* can vary. For instance, temperature and pressure-induced changes have been identified by several authors to shift *Eg*, cause phase transitions and change the bandgap nature from direct to indirect [24, 25, 26, 27]. However, it is the bandgap tuning via modification of the concentrations of metal cation [28, 29] and the halide anion [30, 31] that has the strongest effect. Purposely, surface defects have been suggested to dominate ion migration in lead-halide perovskites [32] which relate to intrinsic and extrinsic ion concentrations [33].

The contributions of ion migration and recombination to the *J-V* hysteresis are typically approached in operational conditions, under 1 sun illumination [34]. In contrast, working in dark conditions implies lower concentration of charge carriers and thus a main contribution from radiative and non-radiative SRH recombination to the total device current [35, 36]. In addition, the electrical response of the samples in dark conditions is simpler due to their lower sensitivity to thermal and

⋆The authors acknowledge support from the project PID2022-139586NB-C44 funded by MCIN/AEI/10.13039/501100011033 and FEDER, EU.

*Corresponding author.
Email addresses: tejada@ugr.es (J. A. Jiménez-Tejada), mgar3705@gmail.com (M. García-Rosell), osbel.almora@urv.cat (O. Almora), pilar.lopez-varo@ipvf.fr (P. López-Varo)

radiative processes favored under illumination. Moreover, with photogeneration, the charge carrier increase favors instability [37, 38], and exotic behaviors, such as the high low-frequency capacitance [39], strong-coupling polarons [40], trions [40, 41], and photo-bleaching shift [42].

The influence of light-induced degradation and enhanced ion-related phenomena on the J-V curve hysteresis of PSCs can be circumvented, to some extent, by studying dark conditions [43, 44]. Furthermore, one can also combine impedance spectroscopy (IS) and current density-voltage $J-V$ curves in dark, where the hysteresis can be explained as a combination of capacitive and non-capacitive currents [45, 21, 46, 47]. Specifically, it has been proposed that the dark capacitive hysteretic currents are associated to the formation of space-charge regions close to the interfaces, which also produce an increase in the low-frequency capacitance [48]. Moreover, several experiments suggest that different CTLs can impact significantly the hysteretic currents and the capacitance spectra in PSCs [49].

The analysis of the physical origin of the capacitive currents requires detailed modeling and simulation of the pvk/CTL interfaces. For instance, drift-diffusion (DD) numerical simulations have been systematically reported on PSCs under illumination [11, 12, 13, 14, 15, 16, 17] or in dark conditions[11, 12, 13]. Notably, O'Kane [13] studied the relation between ion migration and the value of transient currents due to the variation of biasing in dark conditions. Similarly, Garcia-Belmonte and co-workers have simulated the long term dark current drift and diffusion regimes in millimeter-thick perovskite samples in the dark [50, 51, 52]. However, to the best of our knowledge, a systematic DD modeling of the dark $J-V$ curve of PSCs, with focus on the interplay between ion migration and the different recombination mechanisms at the pvk/CTL interfaces, is still missing.

In this work, the effect of ion migration and electronic recombination at the interfaces on the performance of PSCs under dark conditions is studied. A previously developed DD model [16] for a typical PSC structure (see Fig. 1) is considered, in which the perovskite layer is sandwiched between the electron and hole transport layers (ETL and HTL, respectively) and different recombination mechanisms proposed in the literature are included [15, 53, 54]. In addition, we model the pvk/CTL interface as a buffer layer with a non-zero thickness, characterized by its own effective bandgap energy, in which band-to-band or SRH recombination take place. This model is able to reproduce experimental hysteresis of $J-V$ curves in dark conditions. Our proposal and other charge transfer models are detailed in Section 2. The methodology followed in the simulation work is provided in Section 3. The simulation results are shown and discussed in Section 4. Finally, the conclusions are drawn in Section 5.

2. Interface recombination models

A previously developed numerical simulator [55, 56, 20, 16, 57] is used to simulate the behavior of a PSC, which includes DD equations for electronic and ionic charges, the Poisson equation and the continuity equations for electrons and holes. Ion migration is limited only to the perovskite region, discarding possible migration of ions into the selective contacts, e.g., when the device degrades [19]. The solution of these equations determines the distributions of electrons $n(x)$, holes $p(x)$, anions $a(x)$, cations $c(x)$, electron current density $J_n(x)$, hole current density $J_p(x)$, anion current density $J_a(x)$, cation current density $J_a(x)$, electric field $\xi(x)$ and electric potential $\varphi(x)$ at any position x throughout the structure.

The continuity equations for electrons and holes include the recombination rate $R(x)$ and generation rate $G(x)$ terms:

$$\begin{aligned} \frac{dn}{dt} &= \frac{1}{q}\frac{dJ_n}{dx} + G - R \\ \frac{dp}{dt} &= -\frac{1}{q}\frac{dJ_p}{dx} + G - R \end{aligned} \tag{1}$$

where the derivatives are taken with respect to the time (t) and the position (x), and q is the elementary charge. $R(x)$ initially incorporates the band-to-band bulk recombination rate R_B in the perovskite:

$$R(x) = R_B(x) = B_B[n(x)p(x) - n_{i,pvk}^2], \tag{2}$$

where B_B is the bulk recombination coefficient and $n_{i,pvk}$ is the intrinsic charge carrier concentration of the perovskite.

Specific recombination mechanisms in the pvk/CTL interfaces are included with the term R_S, which is restricted to a small region of thickness $\delta \sim 1-5$ nm inside the perovskite and next to the CTLs [53, 15, 58, 59] (see Fig. 2). Therefore, the interface recombination is assumed as:

$$R(x) = R_B(x) + R_S(x). \tag{3}$$

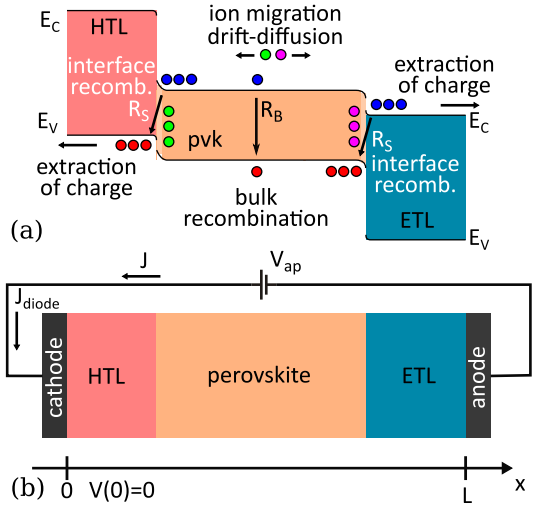

Figure 1: (a) General energy band diagram of the constituent layers of a PSC with different mechanisms included in the simulation. (b) Sign criteria for current J and applied voltage V_{ap} in the PSC. The hole and electron transport layers are HTL and ETL, respectively. The interface and bulk recombination rates are R_S and R_B. The valence and conduction band energy levels are E_V and E_C, respectively, x is the position variable, and L is the distance between electrodes.

In the following sections, different models for the interface recombination rate R_S are introduced and compared. Model 1 and Model 2 are found in the literature [53, 15, 58, 59]. They add the recombination rate R_S inside a small region of the perovskite layer close to perovskite/CTL interface. Our proposals are named Model 3 and Model 4, and the recombination rate R_S is added inside a finite effective buffer region between the perovskite and CTLs, and they consider a crossing charge recombination between the charge carriers from the CTL and the perovskite layer. When the thickness of this buffer region is strictly zero, Models 3 and 4 are equivalent to another approach found in the literature that simulates the interface recombination as a boundary condition at abrupt interfaces [54, 58].

Model 1: (Fig. 2a) Interface recombination is modeled with a band-to-band recombination mechanism in the whole perovskite, only changing inside thin layers close to the pvk/CTL interfaces with interface recombination coefficient B_S, much higher than the bulk recombination coefficient B_B. This model has been used in previous works [53, 15]. The global recombination rate (3) is taken as:

$$\begin{aligned} R(x) &= R_B(x) + B_S[n(x)p(x) - n_{i,pvk}^2]W(x) \qquad (4) \\ W(x) &= \begin{cases} 1, & x \in [x_{HTL/pvk}, x_{HTL/pvk} + \delta] \\ & \cup [x_{pvk/ETL} - \delta, x_{pvk/ETL}] \\ 0, & \text{rest of cases} \end{cases} \end{aligned}$$

where $x_{HTL/pvk}$ and $x_{pvk/ETL}$ are the positions of the HTL/pvk and pvk/ETL interfaces, respectively.

Model 2: (Fig. 2b) Unlike Model 1, in Model 2 the $\delta \sim 1-5$-thick region near the CTLs only recombines through a SRH recombination mechanism, assisted by recombination centers located in the perovskite midgap $E_T = Eg_{,pvk}/2$. This scenario has also been considered in different works [58, 59]. The total recombination rate is then defined as:

$$\begin{aligned} R(x) &= R_B(x) + \frac{[n(x)p(x) - n_{i,pvk}^2]}{\tau_p[n(x) + n_1] + \tau_n[p(x) + p_1]} W(x) \qquad (5) \\ W(x) &= \begin{cases} 1, & x \in [x_{HTL/pvk}, x_{HTL/pvk} + \delta] \\ & \cup [x_{pvk/ETL} - \delta, x_{pvk/ETL}] \\ 0, & \text{rest of cases} \end{cases} \end{aligned}$$

where n_1 and p_1 are the effective electron and hole concentrations evaluated when the Fermi level is at level E_T, and τ_n and τ_p are the trapping time constants for electrons and holes, respectively.

Model 3: (Fig. 2c) An alternative to the previous Model 1, is now proposed with Model 3 with a similar main contribution from the radiative recombination. Distinctively, an effective intrinsic charge carrier density $n_{i,eff}$ and an effective bandgap energy Eg_{eff} are assumed at the interface buffer layers. Particularly, Eg_{eff} is defined as the energy difference between the border of the perovskite conduction/valence band and the border of the CTL valence/conduction band for the pvk/CTL interfaces ($Eg_{eff} = Ec_{,pvk} - Ev_{,HTL}$ for the HTL/pvk interface and $Eg_{eff} = Ec_{,ETL} - Ev_{,pvk}$ for the pvk/ETL interface). For simplicity, we consider the same value of Eg_{eff} for both pvk/CTL interfaces. The value of Eg_{eff} defines an ef-

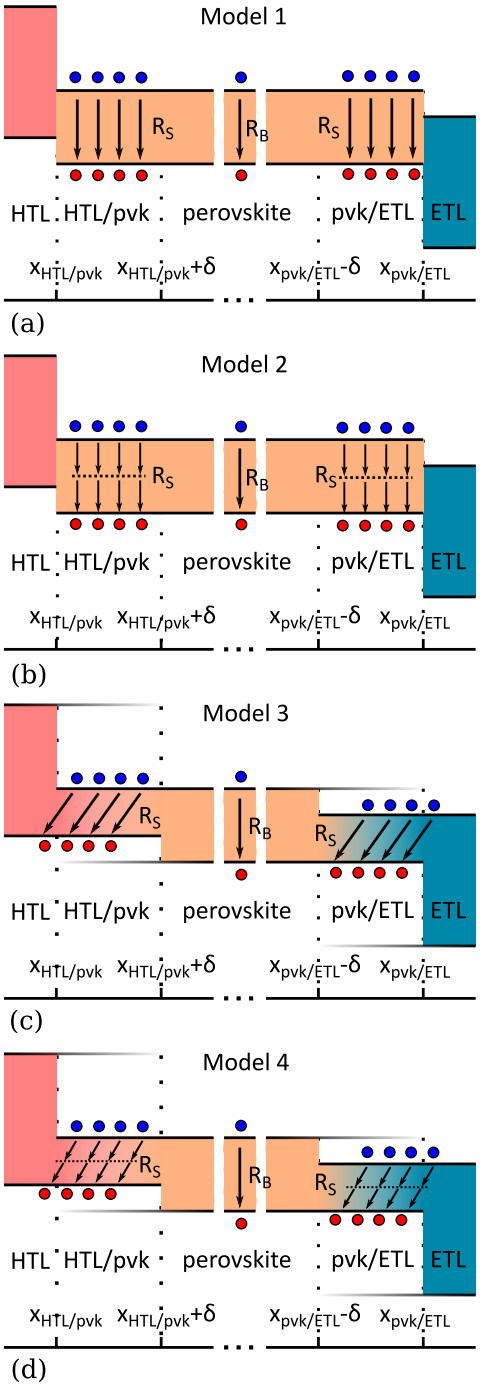

Figure 2: Different recombination models that describe specific recombination at the pvk/CTL interfaces. a) Radiative band-to-band recombination close to the interface, b) Shockley-Read-Hall (SRH) non-radiative recombination close to the interface, c) Radiative band-to-band recombination in a buffer interface layer, d) SRH non-radiative recombination in a buffer interface layer.

fective intrinsic carrier density for these buffer interface layers, $n_{i,eff_{HTL/pvk}} = n_{i,eff_{pvk/ETL}} = n_{i,eff}$, with:

$$n_{i,eff} = n_{i,pvk} \exp[(Eg_{,pvk} - Eg_{eff})/(2kT)]. \quad (6)$$

These virtual layers model the crossed recombination between the majority charge carriers in the CTLs and their respective opposite-sign charge carriers in the perovskite (holes in the HTL with electrons in the perovskite at the HTL/pvk interface, and electrons in the ETL with holes in the perovskite at the pvk/ETL interface) (see Fig. 2c). Importantly, the interface recombination rate R_S in Model 3 is modeled as a band-to-band recombination mechanism in which the local concentrations of electrons and holes are substituted by their respective mean values $< n >_j$ and $< p >_j$. Then, the corresponding total recombination rate results:

$$\begin{aligned} R(x) &= R_B(x) \\ &+ W(x) \sum_{j=pvk/ETL}^{HTL/pvk} B_{S_j}(< n >_j < p >_j - n^2_{i,eff_j}) \\ W(x) &= \begin{cases} 1, & x \in [x_{HTL/pvk}, x_{HTL/pvk} + \delta] \\ & \cup [x_{pvk/ETL} - \delta, x_{pvk/ETL}] \\ 0, & \text{rest of cases} \end{cases} \end{aligned} \quad (7)$$

and the mean values are calculated in the δ-thick regions near the pvk/CTL interfaces as:

$$\begin{aligned} < n >_{HTL/pvk} &= \frac{1}{\delta} \int_{x_{HTL/pvk}}^{x_{HTL/pvk}+\delta} n(x)dx \\ < p >_{HTL/pvk} &= \frac{1}{\delta} \int_{x_{HTL/pvk}-\delta}^{x_{HTL/pvk}} p(x)dx \\ < n >_{pvk/ETL} &= \frac{1}{\delta} \int_{x_{pvk/ETL}}^{x_{pvk/ETL}+\delta} n(x)dx \\ < p >_{pvk/ETL} &= \frac{1}{\delta} \int_{x_{pvk/ETL}-\delta}^{x_{pvk/ETL}} p(x)dx \end{aligned} \quad (8)$$

The crossed recombination between minority carriers of the CTLs and the respective opposite-sign charge carriers in the perovskite is neglected in (7), since the concentration of the minority carriers in the CTLs is extremely low, due to the large band gap of the CTLs. Notably, the value of the thickness δ affects the width of the hysteresis loop in the $J-V$ curves, as is detailed in Section 4.4.

The term n^2_{i,eff_j} (6), included in our band-to-band cross-recombination model (7), can be neglected under illumination when the cross-products ($< n >_j < p >_j$) are very large due to the high accumulation of free charges around the interfaces. This also applies to interface cross-recombination models which have been used in the past in PSCs under illumination without this effective term [16]. However, under dark steady-state short-circuit (i.e., $V_{ap} = 0$ V) conditions, unrealistic current density (i.e. $J \neq 0$) values arise if the n_{i,eff_j} term is neglected. This can be seen in the blue curves of Fig. S4a in the Supporting Information (SI).

Model	Interface recombination in δ-layer	n_i	Refs.
1	$B_S = 10^{-6} cm^3 s^{-1}$	$n_{i,pvk}$	[53, 15]
2	$\tau_n = \tau_p = 1$ ms	$n_{i,pvk}$	[58, 59]
3	$B_S = 10^{-14} cm^3 s^{-1}$	n_{i,eff_j}, (6)	this work
4	$\tau_n = \tau_p = 1$ ms	n_{i,eff_j}, (6)	this work

Table 1: Main parameters used in Models 1-4

Model 4: (Fig. 2d) This model employs the same n^2_{i,eff_j} (6) and Eg_{eff} assumptions introduced for Model 3, only that poses an alternative to Model 2, where the interface recombination rate R_S in (7) is considered due to a SRH recombination mechanism, assisted by recombination centers located in the effective buffer layer midgap $E_T = Eg_{eff}/2$ (or $n_{1_j} = p_{1_j} = n_{i,eff_j}$ in (9)). Therefore, the total recombination rate is taken as:

$$\begin{aligned} R(x) &= R_B(x) \\ &+ W(x) \sum_{j=pvk/ETL}^{HTL/pvk} \frac{< n >_j < p >_j - n^2_{i,eff_j}}{\tau_p(< n >_j + n_{1_j}) + \tau_n(< p >_j + p_{1_j})}, \\ W(x) &= \begin{cases} 1, & x \in [x_{HTL/pvk}, x_{HTL/pvk} + \delta] \\ & \cup [x_{pvk/ETL} - \delta, x_{pvk/ETL}] \\ 0, & \text{rest of cases} \end{cases} \end{aligned} \quad (9)$$

The four models are summarized in Table 1, where the main differences are displayed in terms of the interface recombination in the δ-thick layers between the perovskite and the CTLs, and the use of the effective bandgap approximation for the intrinsic charge carrier density, n_i.

3. Simulation method and initial tests

This work aims to complement the analysis of experimental $J-V$ curves with hysteresis, measured in PSCs in dark conditions, with an interface model for better understanding of the J-V hysteresis in these curves. Particularly, $J-V$ curves measured in PSCs in dark conditions at a high voltage sweep scan rates (>1V/s), and showing a hysteresis loop around $V_{ap} = 0$ V, are considered as the main study case [21, 45]. These are convenient conditions for which the distribution of mobile ions can be assumed nearly invariant during the whole voltage sweep. This eases the incorporation of the interface recombination Models 1-4 (4)-(9) into the DD simulator [16]. Then, $J-V$ curves at high voltage sweep scan rates are calculated according to the following procedure:

(i) The invariant distribution of ions is calculated numerically in steady-state conditions at the initial value of the bias voltage. Using this invariant distribution of ions, a "fast" $J-V$ curve is calculated. An example of initial ion distributions is seen in Figs. S1c-S1d in the SI. (ii) The current is evaluated from negative to positive bias voltages (reverse-forward (RF) sweep). (iii) The current is evaluated in the reverse way (forward-reverse (FR) sweep). In the figures of this work, the RF and FR curves

are depicted with solid and dashed lines, respectively. The values of the parameters used in the numerical simulations are shown in Table S1 in the SI.

3.1. Initial tests

Prior to the analysis of the interface recombination models, some initial tests are performed. First, a PSC with mobile cations and anions with concentration $N_{ion} = 5 \times 10^{17}$ cm^{-3} was simulated, including bulk recombination mechanisms ($R = R_B \neq 0$) with a bulk recombination coefficient $B_B = 5 \times 10^{-11} cm^3 s^{-1}$, but neglecting specific recombination mechanisms at the interfaces ($R_S = 0$). Figure 3 shows the energy band diagrams and the distribution of electrons, holes, anions, and cations in equilibrium ($V_{ap} = 0$ V) and dark conditions for this reference sample.

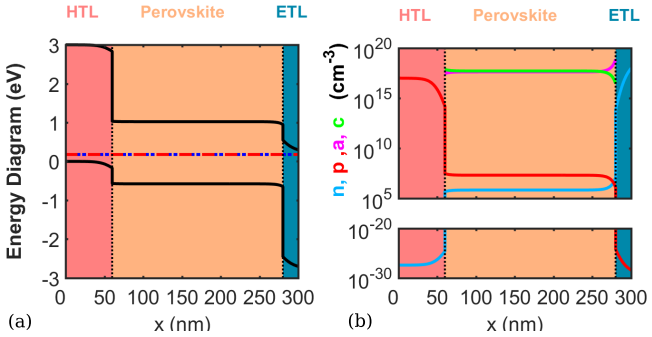

Figure 3: (a) Energy bands and (b) distribution of ions and free charge carriers calculated for the PSC in equilibrium and dark conditions using the parameters shown in Table S1 ($R = R_B \neq 0$, $R_S = 0$)

The fast J–V curves in dark conditions for this reference case are shown with gray lines in Fig. 4. They are used as a reference for comparison with other $J - V$ curves calculated in this work. These same curves are represented apart in Figs. S1a-S1b to check the nonexistence of hysteresis under these conditions: $N_{ion} \neq 0$, $R = R_B \neq 0$, $R_S = 0$. Importantly, the presence of mobile ions is a necessary but not sufficient condition for the $J - V$ curve hysteresis to occur. Only under particular ranges of numerical parameters, the RF and FR sweeps result different.

The second test studies the effect of the value of B_B, which modulates the bulk recombination in the perovskite (2). This test, which is detailed in SI (Section S2), concludes that no significant hysteresis is detected in the calculated fast $J - V$ curves when $B_B \leq 5 \times 10^{-7}$ cm^{3}s^{-1} and $N_{ion} \leq 5 \times 10^{17}$ cm^{-3} (see Fig. S2). The values of B_B used in the test agree with previous reports in the literature [60] and lie within the range $[5 \times 10^{-11}, 5 \times 10^{-7}]$ cm^{3}s^{-1}. These values are smaller than the Langevin rate evaluated for the perovskite [61] $B_{Langevin} = q(\mu_e+\mu_h)/\epsilon = 1.4{\times}10^{-6}$ cm^{-3}s^{-1} with electron mobility $\mu_e = 10$ cm^2/(Vs), hole mobility $\mu_h = 10$ cm^2/(Vs), and dielectric constant $\epsilon = 2.3 \times 10^{-12}$ F/cm [16, 62, 63]. Furthermore, in the rest of this work, the value of B_B is kept constant at $B_B = 5 \times 10^{-11}$ cm^{3}s^{-1}, including the reference sample (gray $J - V$ curves in Fig. 4).

The third test checks the physical validity of the interface recombination Models 1–4 through the condition of equilibrium ($V_{ap} = 0$ V without photon generation) which must strictly be $J = 0$ A/cm^2. This condition is validated in SI (Section S3) for the four models.

Also in this Section S3, some examples of apparently good interface recombination models, that do not fulfill this condition, are presented, but consequently ignored.

After these initial tests, the following simulations and studies are made in order to reproduce the type of hysteresis observed in some experimental $J - V$ curves [45, 21, 46]: simulation of fast $J - V$ curves including in the DD simulator the interface recombination Models 1–4, in (i) both interfaces, and (ii) only one interface; and study of the effects of (iii) the interface recombination coefficient B_S and the interface trapping time constants $\tau_n (= \tau_p)$; (iv) the thickness δ of the buffer interface recombination layer; (v) the concentration of ions N_{ion}; (vi) the band alignment at the pvk/CTL interfaces, $Ev,_{HTL} - Ev,_{pvk}$ and $Ec,_{pvk} - Ec,_{ETL}$, and (vii) the current leakages. The results of these studies are discussed in the next section.

4. Results

4.1. Interface recombination in both pvk/CTL interfaces.

Figure 4 shows fast $J - V$ curves in dark conditions, calculated with the four interface recombination models for R_S, with $B_B = 5 \times 10^{-11}$ cm^{3}s^{-1} and $N_{ion} = 5 \times 10^{17}$ cm^{-3}. The four models are computed in a $\delta = 5$ nm thickness region located close to both pvk/CTL interfaces. Model 1 (4) uses $B_S = 10^{-6}$ cm^{3}s^{-1} $\gg B_B$ in Fig. 4a; Model 2 (6) considers a recombination center with $\tau_n = \tau_p = 1$ ms in Fig. 4b; Model 3 (7) uses $B_S = 10^{-14}$ cm^{3}s^{-1} $\ll B_B$ in Fig. 4c; and Model 4 considers a recombination center with $\tau_n = \tau_p = 1$ ms in Fig. 4d. The values of these parameters are chosen with the aim to achieve similar current density levels in all the $J - V$ curves. In fact, the value of B_S in Model 1 was intentionally increased in order to detect significant changes between the $R_S = 0$ and $R_S \neq 0$ cases.

In Figure 4, the gray curve corresponds to a reference case with no interface recombination ($R_S = 0$). In the four cases of Fig. 4, the magnitude of current density evaluated with $R_S \neq 0$ is always greater or equal to the magnitude of the current evaluated with $R_S = 0$ (gray curves).

In Model 1, there is no hysteresis loop around 0 V (Fig. 4a), only a small one is observed at high bias voltages, similar to that observed in Fig. S2b when B_B is increased to the highest value. In Fig. 4b (Model 2) a small hysteresis loop is observed at low positive bias voltages. In both Fig. 4c (Model 3) and Fig. 4d (Model 4), a larger hysteresis loop is observed, spreading to the whole range of positive values of V_{ap}, and changing the sign of the current density at V_{ap} around 0 V.

The analysis of the four sets of curves in Fig. 4 suggests that (i) the small differences shown in the $J - V$ curves calculated with Models 1 and 2 are due to the different relation between R_S and the free charge density $[n(x), p(x)]$. Specifically, Model 1 shows a quadratic relation [$\propto (cm^{-3})^2$ in (4)]

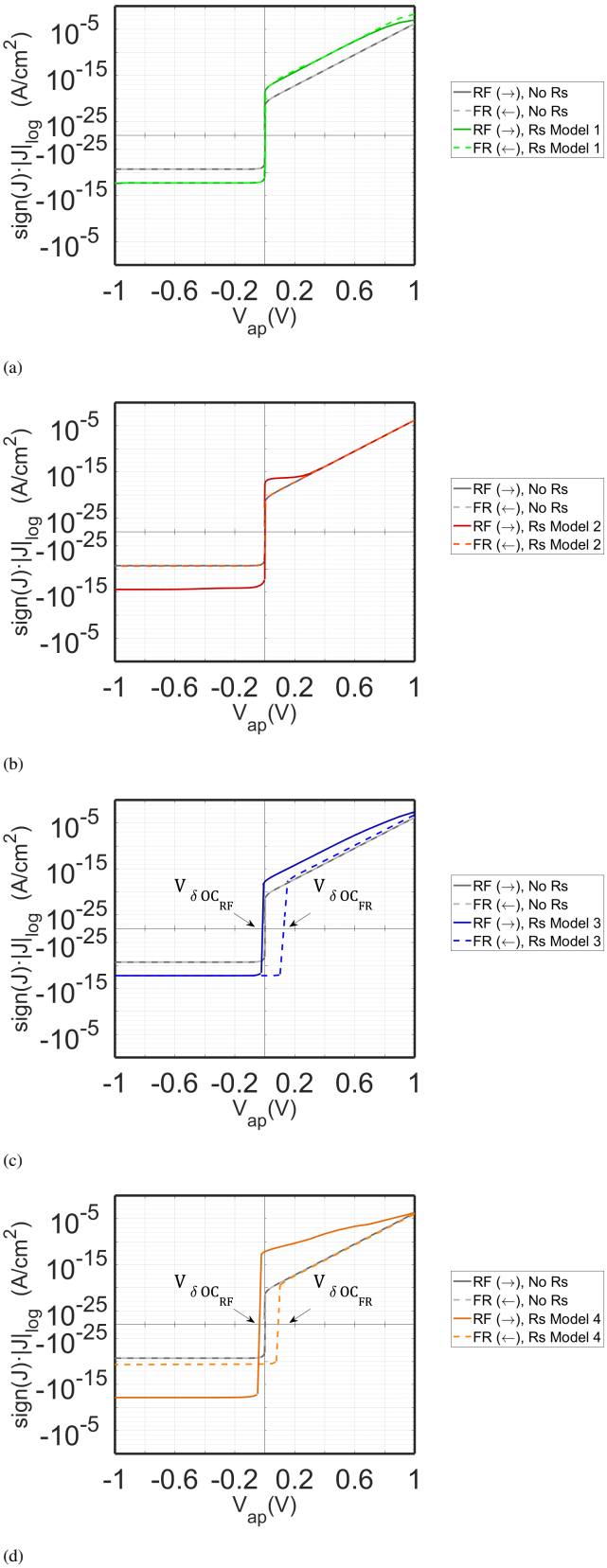

Figure 4: Semi-logarithmic fast $J-V$ curves, calculated with $B_B = 5\times10^{-11}$ cm^{3}s^{-1} and the four interface recombination models for R_S. In the four models, $\delta = 5$ nm. (a) Model 1 with $B_S = 10^{-6} cm^3 s^{-1}$; (b) Model 2 with $\tau_n = \tau_p = 1$ ms; (c) Model 3 with $B_S = 10^{-14} cm^3 s^{-1}$; (d) Model 4 with $\tau_n = \tau_p = 1$ ms. As a reference in all the figures, the gray curves represent the case with $R_S = 0$.

and Model 2 shows an almost linear one [$\propto (cm^{-3})^1$ in (6)]. (ii) Only Models 3 and 4, based on an interface buffer region, are able to produce a significant hysteresis loops around $V_{ap} = 0$ V, similar to those ones observed in experimental measurements [21, 45, 46]. The lower voltage of the loop, or the value of V_{ap} at which the current in the RF curve changes its sign, is named $V_{\delta OC_{RF}} < 0$, and the upper voltage of the loop, or the value of V_{ap} at which the current in the FR curve changes its sign, is $V_{\delta OC_{FR}} > 0$. The width of the hysteresis loop is defined as $V_{\delta OC} = V_{\delta OC_{FR}} - V_{\delta OC_{RF}}$. In Fig. 4, $V_{\delta OC} \approx V_{\delta OC_{FR}}$, since $V_{\delta OC_{RF}} \approx 0$. This characteristic voltage indicates a transient open-circuit voltage that depends on the scan rate.

Notably, the value of B_S in Model 3 is eight orders of magnitude lower than the one used in Model 1, and the values of the time constants τ_n and τ_p used in Model 4 are the same as those in Model 2. In the next sections we focus the discussion only on our proposals for interface recombination models; i.e., models 3 and 4. For completeness, the results for models 1 an 2 can be found in the SI.

4.2. *Effect of B_S and τ_n (= τ_p)*

$J-V$ curves were calculated for different values of B_S and τ_n (= τ_p) in the four models, highlighting the following observations (see Fig. 5 and Fig. S6). The magnitude of the current density increases when B_S increases [Model 1 (Fig. S6a) and Model 3 (Fig. 5a)], or when τ_n (= τ_p) decreases [Model 2 (Fig. S6b) and Model 4 (Fig. 5b)]. No hysteresis loop around $V_{ap} = 0$ V is observed in Models 1-2 (Fig. S6). In Model 3, the width of the hysteresis loop around $V_{ap} = 0$ V increases and the symmetry is lost when B_S increases (Fig. 5a). In Model 4, the hysteresis loop around $V_{ap} = 0$ V increases and the symmetry is lost when the value of τ_n (= τ_p) decreases (Fig. 5b). These behaviors are consistent with the recombination-limited nature of the dark current in forward bias.

4.3. *Recombination models applied to separate interfaces.*

The four models lead to similar hysteresis results, regardless on whether one or the two interfaces are considered. For models 3 and 4, a significant hysteresis is found around $V_{ap} = 0$ V (see Fig. 4) and (Fig. S7). Minor changes are observed when considering the interface recombination model in only one interface, such as: a decrease of the absolute value of the current due to a decrease of the recombination losses; and slight variation in the asymmetry of the hysteresis loop around $V_{ap} = 0$ V (Figs. S7e-h). These minor changes highlight the difficulty of determining which interface or interfaces produce the bottleneck of the current. The complete results can be seen in the SI (Section S5).

4.4. *Effect of the thickness δ*

Fast $J-V$ curves from models 3 and 4, are shown in Figures 6a and 6b, respectively, considering both interfaces with different values of the thickness δ of the effective layer in which the recombination model for R_S is computed ($\delta \in [0, 5]$ nm). For clarity, the same curves are represented separately in SI (Figs. S8a-e and S9a-e) and in linear scale in Figs. S10a-b.

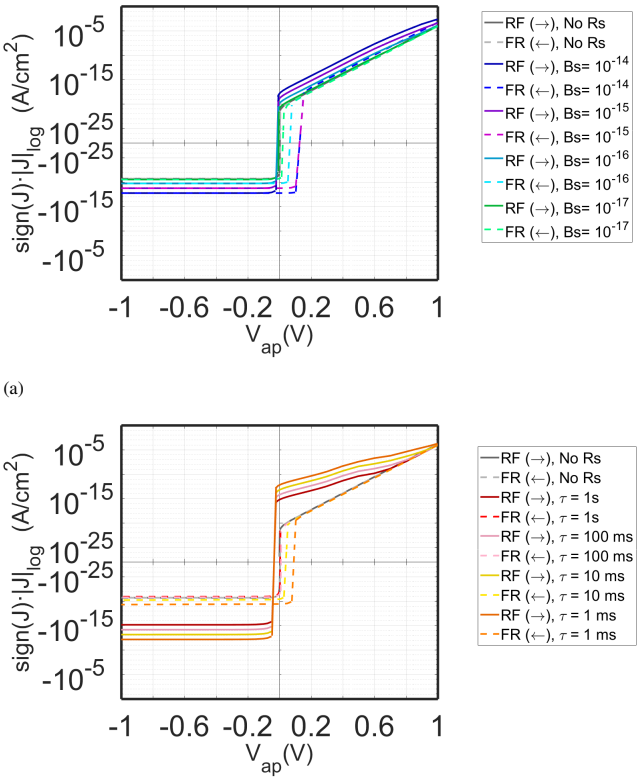

Figure 5: $J-V$ curves calculated using the interface recombination (a) Model 3 for different values of B_S ($[10^{-17}, 10^{-14}]$ cm^{3}s^{-1}) and (b) Model 4 for different values of τ_n ($= \tau_p$) ([1, 1000] ms). The reference case, $R_S = 0$, is in gray lines.

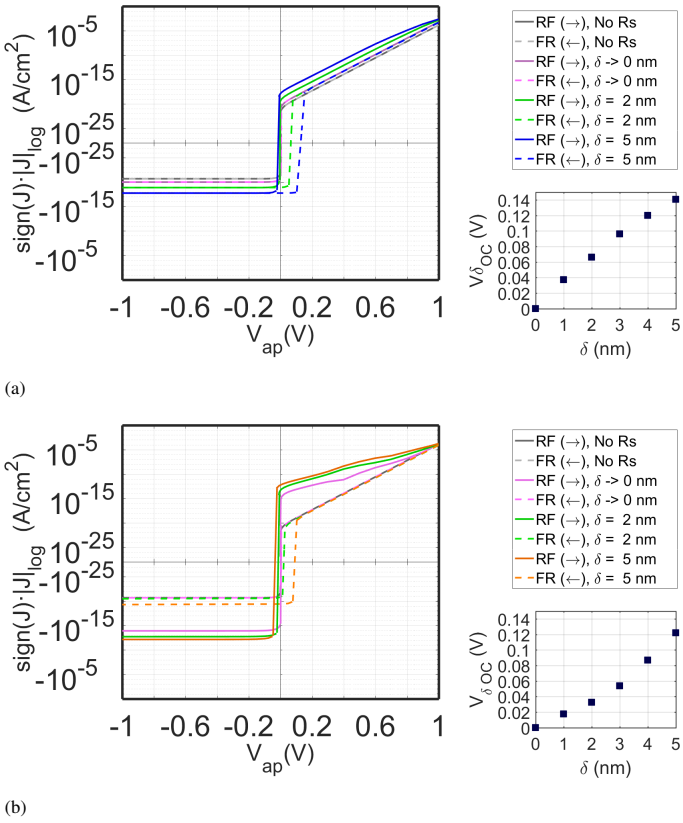

Figure 6: Fast $J-V$ curves calculated for different values of δ in the range [0, 5] nm with $N_{ion} = 5\times10^{17}$ cm^{-3} and $B_S = 10^{-14}$ cm^{3}s^{-1} using the interface recombination Models 3 (a) and 4 (b). They are represented separately in Figs. S8-S9 and in linear scale in Fig. S10. The reference case, using the same concentration of ions and $R_S = 0$, is in gray lines. The insets placed out of the figures show the evolution of $V_{\delta OC}$ with δ.

When $\delta \to 0$, the interface recombination is introduced in the simulator as a boundary condition for the electron and hole current densities at both interfaces:

$$\begin{aligned} J_n(x^-_{HTL/pvk}) - (-q)R_{ss}(x^+_{HTL/pvk}) &= J_n(x^+_{HTL/pvk}) \\ J_p(x^-_{HTL/pvk}) - qR_{ss}(x^+_{HTL/pvk}) &= J_p(x^+_{HTL/pvk}) \\ J_n(x^-_{pvk/ETL}) - (-q)R_{ss}(x^-_{pvk/ETL}) &= J_n(x^+_{pvk/ETL}) \\ J_p(x^-_{pvk/ETL}) - qR_{ss}(x^-_{pvk/ETL}) &= J_p(x^+_{pvk/ETL}) \end{aligned} \tag{10}$$

where R_{ss} for Model 3 is:

$$\begin{aligned} R_{ss}(x^+_{HTL/pvk}) &= \Delta x B_S [n(x^+_{HTL/pvk})p(x^-_{HTL/pvk}) - n^2_{i,eff_{HTL/pvk}}] \\ R_{ss}(x^-_{pvk/ETL}) &= \Delta x B_S [n(x^+_{pvk/ETL})p(x^-_{pvk/ETL}) - n^2_{i,eff_{pvk/ETL}}] \end{aligned} \tag{11}$$

and R_{ss} for Model 4 is:

$$\begin{aligned} R_{ss}(x^+_{HTL/pvk}) &= \Delta x \frac{n(x^+_{HTL/pvk})p(x^-_{HTL/pvk}) - n^2_{i,eff_{HTL/pvk}}}{\tau_p[n(x^+_{HTL/pvk}) + n_1] + \tau_n[p(x^-_{HTL/pvk}) + p_1]} \\ R_{ss}(x^-_{pvk/ETL}) &= \Delta x \frac{n(x^+_{pvk/ETL})p(x^-_{pvk/ETL}) - n^2_{i,eff_{pvk/ETL}}}{\tau_p[n(x^+_{pvk/ETL}) + n_1] + \tau_n[p(x^-_{pvk/ETL}) + p_1]} \end{aligned} \tag{12}$$

Similar boundary conditions have been implemented before in interface recombination models [54, 58]. Note that in (10) the buffer region is reduced to zero. For comparison purposes, a value for the effective thickness of the interface recombination $\Delta x = 0.1$ nm has been chosen in order to achieve a similar order of magnitude in the current density in all the $J-V$ curves. Higher values were tested, obtaining the same conclusions.

When δ decreases, three main features arise for models 3 and 4, as illustrated in Fig. 6, and Figs. S8-S10.

First, at reverse bias voltages, ($V_{ap} \in [-1, 0]$ V), the magnitude of the current decreases slightly in both RF and FR directions of the J-V curves. This can be associated with a reduction of recombination current proportional to the width of the active region where recombination takes place. For any value of δ, including $\delta \to 0$, the magnitude of this current density is greater than in the reference case ($R_S = 0$, gray curve in Fig. 6).

Second, the values of $V_{\delta OC_{FR}}$ and $V_{\delta OC_{RF}}$ decrease in magnitude when δ decreases. In the RF direction, the value of $V_{\delta OC_{RF}}$ is very small and can be better distinguishable in linear scale in Fig. S10. The width of the hysteresis loop $V_{\delta OC}$ decreases with δ at a rate of ~ 0.025 V/nm, being zero at $\delta = 0$ (see insets placed out of Figs. 6a-6b).

Third, at forward bias voltages, ($V_{ap} \in [0, 1]$ V), the current

decreases in the RF direction of the J-V curve, compared to that in the FR direction. In addition the FR curve does not change for $V_{ap} > V_{\delta OC}$ (see also the linear representation in Fig. S10).

The most important observation is the dependence of the hysteresis-loop width $V_{\delta OC}$ with the thickness δ of the buffer layer in which the interface recombination is evaluated. Note that in all of these simulations, the shunt resistance has been neglected, being included in Section 4.7).

4.5. *Effect of the ion concentration N_{ion}*

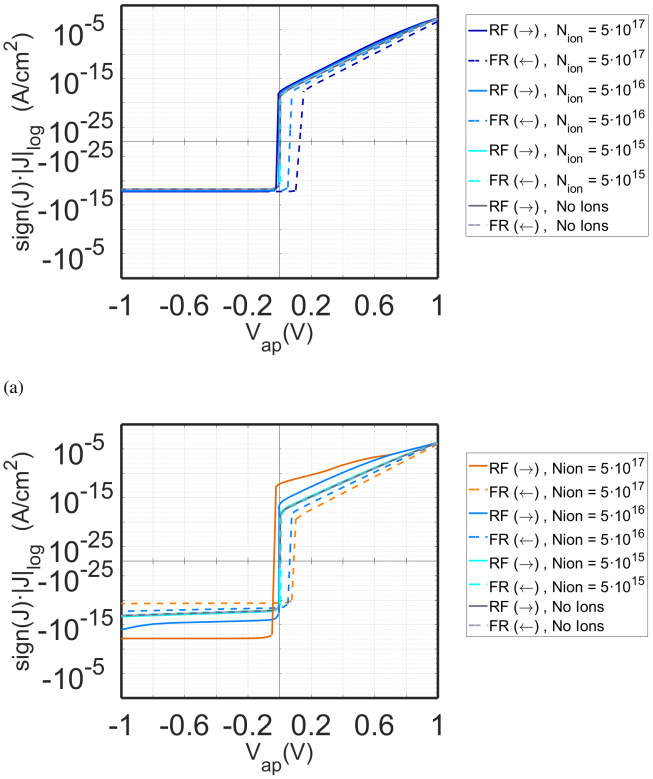

(a)

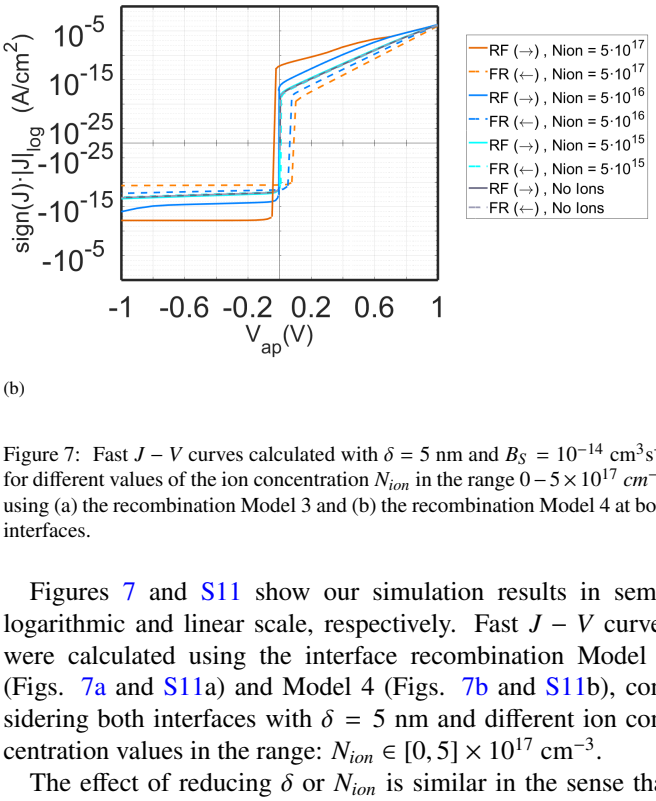

(b)

Figure 7: Fast $J-V$ curves calculated with $\delta = 5$ nm and $B_S = 10^{-14}$ cm^{3}s^{-1} for different values of the ion concentration N_{ion} in the range $0-5\times10^{17}$ cm^{-3}, using (a) the recombination Model 3 and (b) the recombination Model 4 at both interfaces.

Figures 7 and S11 show our simulation results in semi-logarithmic and linear scale, respectively. Fast $J-V$ curves were calculated using the interface recombination Model 3 (Figs. 7a and S11a) and Model 4 (Figs. 7b and S11b), considering both interfaces with $\delta = 5$ nm and different ion concentration values in the range: $N_{ion} \in [0,5]\times10^{17}$ cm^{-3}.

The effect of reducing δ or N_{ion} is similar in the sense that the hysteresis loop $V_{\delta OC}$ is reduced when decreasing δ or N_{ion}. Neglecting the buffer layer at $\delta = 0$ or ion migration at $N_{ion} = 0$ cm^{-3}, cancels the hysteresis, leading to the same RF and FR J-V curves, and $J(V_{ap} = 0V) = 0$ A/cm^2. However, further differences are observed for the dependency of dark hysteresis on the mobile ion density.

In the reverse bias range $V_{ap} \in [-1,0]$ V, for Model 3, the magnitude of the current density decreases in both RF and FR sweeps (Fig. 7a). This is seen more clearly in Fig. S11a. This decrease is lower than that when diminishing the value of δ. In contrast, for Model 4 in the same range, the current density increases in the FR sweep, unlike the effect of diminishing δ, where $|J|$ decreases in the FR sweep.

In the bias range of values higher than that of the hysteresis transient open-circuit voltage $V_{ap} > V_{\delta OC_{FR}}$, the magnitude of the current is reduced in the RF curves but is increased in the FR ones, for both models 3 and 4. When reducing δ in the FR sweep, $|J|$ does not change. These differences can be correlated with the dependency of the effective built-in voltage on the value of N_{ion} . Higher concentrations of mobile ions affect the concentration of free charge carriers changes at the interface, modifying the value of the interface recombination rate as well, and introduces field screening [51, 64, 65].

4.6. *Effect of the built-in voltage*

This section analyzes the effect of modifying the built-in voltage by varying the band alignment between the CTLs and the perovskite layer. The $J-V$ curves are calculated using the interface recombination models 3 and 4. The built-in voltage is modified by a shift on the electron affinity (E_a) of the CTLs, altering the band gap effective value Eg_{eff} and the effective intrinsic concentration $n_{i,eff}$ of both buffer layers in which models 3 and 4 are evaluated (Figs. 8a and 8b). For simplicity, the values of the doping densities N_A, N_D and the energy band gap Eg of all the layers are kept invariant. Moreover, the changes of the electronic affinities $E_{a,HTL}$ and $E_{a,ETL}$ of the CTLs, referred to a common vacuum level E_o, are the same in magnitude but opposite in sign ($\Delta E_{a,HTL} = -\Delta E_{a,ETL} > 0$), and then, the value of Eg_{eff} is also the same in both interfaces (Figs. 8a and 8b). Since the parameters of the perovskite do not change, the energy bands of the CTLs are vertically displaced in relation to the energy bands of the perovskite: the HTL energy bands downwards and ETL ones upwards (the energy bands of the separate layers for three cases cases are represented in Figs. 8a and 8b).

The electron affinities of the selective contacts of these three PSCs are: $E_{a,HTL} + \Delta E_a$ and $E_{a,ETL} - \Delta E_a$ with ΔE_a =0.1, 0.25 and 0.4 eV, where $E_{a,HTL}$ and $E_{a,ETL}$ correspond to the case studied in Fig. 4, in which $V_{bi} = 0.5$ V and $Eg_{eff} = 1.2$ eV. The values of V_{bi} and Eg_{eff} of these three cases are: (a) $V_{bi} = 0.7$ V, $Eg_{eff} = 1.3$ eV; (b)$V_{bi} = 1.0$ V, $Eg_{eff} = 1.45$ eV; and (c) $V_{bi} = 1.3$ V, $Eg_{eff} = 1.6$ eV.

Figures 8c-8h show the $J-V$ curves calculated, using Model 3 (left column) and Model 4 (right column), for the three cases. Other cases can be seen in SI, Section S8. They show how the central hysteresis loop around $V_{ap} = 0$ V is reduced when Eg_{eff} increases toward the limit $Eg_{eff} \rightarrow Eg_{,pvk} = 1.6$ eV, and the built-in voltage increases. Just at $Eg_{eff} = Eg_{,pvk}$ (or $n_{i,eff} = n_{i,pvk}$, $V_{bi} = 1.3$ V), this loop disappears when using Model 3 (Fig. 8g), but it still persists when using Model 4 (Fig. 8h). The hysteresis loop also diminishes at high values of V_{ap}.

Discontinuities in the energy bands at the interfaces (cases in Figs. 8c-8f) make charge carriers accumulate at these interfaces. These accumulated charges are involved on the recombination mechanisms at the interface and the recombination losses are significant. Devices with higher built-in volt-

ages need higher mobile ion concentrations to screen the internal electric field and modify the charge accumulation close to the interfaces around short-circuit condition.

The analysis of Fig. 7 shows that the presence of mobile ions is needed for hysteresis to occur in any range of V_{ap}. Nevertheless, other requirements must be fulfilled in order to detect a hysteresis loop around $V_{ap} = 0$ V. This includes appropriate values for the electron affinity of the PSCs in relation to the perovskite (Fig. 8). Moreover, appropriate values of the interface radiative recombination coefficients (Fig.5a) or SRH interface trapping time constants (Fig. 5b) are also necessary for the hysteresis to be detected.

4.7. Effect of the shunt resistance

In the previous sections, the numerical calculations consider an ideal PSC with no shunt resistance. The total current density J equals the current density through the device J_{diode} ($J = J_{diode}$ in Fig. 1b). The values of the current density obtained so far are quite small compared to experimental values measured in dark conditions [45, 21, 46, 47]. Current leakages J_{leak} through alternative paths are always present in practical situations and can be important in determining the final value of the total current that flows through the device. In these cases, $J = J_{leak} + J_{diode}$.

The current-voltage curve of a single shunt resistor R_{shunt} crosses the abscissa axis ($J = 0$ A/cm^2) at $V_{ap} = 0$ V. However, the $J - V$ curves showing hysteresis loops in Figs. 6a-6b cross the axis $J = 0$ A/cm^2 at voltages $V_{\delta OC_{RF}} < 0$ and $V_{\delta OC_{FR}} > 0$, for the respective RF and FR sweeps. The leakage current J_{leak} must follow the sign of the diode current J_{diode}. Thus, the set of components that models the leakage current must fulfill the conditions: J_{leak}=0 A/cm^2 at $V_{ap} = V_{\delta OC_{FR}}$ in the FR sweep, and J_{leak}=0 A/cm^2 at $V_{ap} = V_{\delta OC_{RF}}$ in the RF sweep. In this regard, the current flowing through this element should be:

$$J_{leak} = \frac{V_{ap}}{R_{shunt}} - \frac{V'}{R_{shunt}} \tag{13}$$

where $V' = V_{\delta OC_{RF}}$ in the RF sweep and $V' = V_{\delta OC_{RF}}$ in the FR one. This is equivalent to a circuit element formed by a shunt resistance R_{shunt} in parallel with a current source V'/R_{shunt}. This parallel combination shunts the PSC, as seen in Fig. 9. Note that the dc circuit model shown in Fig. 9 depends on V', which at the same time depends on the sweep direction and on the scan rate. The difference $V_{ap} - V'$ in (13) provides information about the sign of the effective electric field inside the perovskite.

The effect of the shunt resistance is incorporated on the cases analyzed in Fig. 4: a PSC in dark conditions with ion concentration $N_{ion} = 5 \times 10^{17}$ cm^{-3} inside the perovskite semiconductor, and the interface recombination Models 3 (7) and 4 (9) applied in both interfaces (Models 1 and 2 are not analyzed here since no hysteresis was obtained with them. Please see Figs. S17a-S17b). Adding the effect of a shunt resistance $R_{shunt} = 10^3$ Ω·cm^2, the resulting new $J - V$ curves can be seen in Figs. 10a and 10b, respectively. In these figures, the $J - V$ curves of our reference case with no interface recombination model, are also depicted (gray lines), although hidden underneath the curves that do incorporate the interface model. These gray curves are also represented apart in the SI (Fig. S16b). The value of R_{shunt} used in the simulations is chosen so that the order of magnitude of the calculated curves in Figs. 10a-10b, and the experimental values taken from the literature [45, 21, 46, 47], are similar. The comparison of Figs. 4c-4d and 10a-10b shows that (i) the widths of the hysteresis loops obtained when using Models 3-4, without current leakages (Figs. 4c-4d), or with them (Figs. 10a-10b), remain the same; (ii) slopes in both FR and RF curves are softened in Fig. 10 in comparison to Fig. 4; and (iii) Fig. 10a,

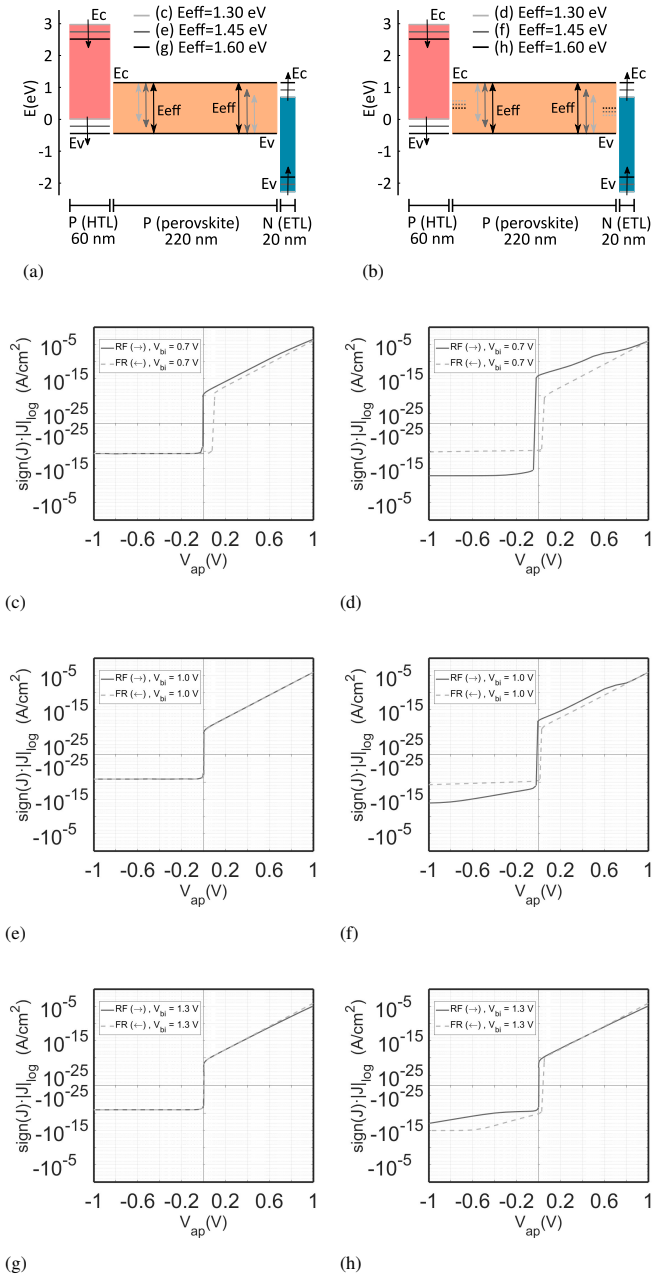

Figure 8: (a)-(b) PSCs with three different energy diagrams (represented for the separate layers in equilibrium). The interface recombination Model 3 (a) and Model 4 (b) are used in both interfaces and $N_{ion} = 5 \times 10^{17}$ cm^{-3}. (c)-(h) Fast $J - V$ curves in logarithmic scale calculated for these three cases: (c)-(d) $V_{bi} = 0.7$ V ($Eg_{eff_{1,2}} = 1.3$ eV), (e)-(f) $V_{bi} = 1.0$ V ($Eg_{eff_{1,2}} = 1.45$ eV), (g)-(h) $V_{bi} = 1.3$ V ($Eg_{eff_{1,2}} = 1.6$ eV).

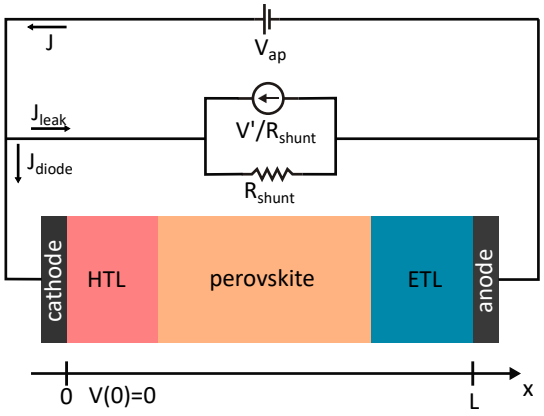

Figure 9: PSC structure including a shunt resistor in the perovskite with J_{leak} defined in (13) and $V' = V_{\delta OC_{RF}}$ in the RF sweep and $V' = V_{\delta OC_{RF}}$ in the FR one.

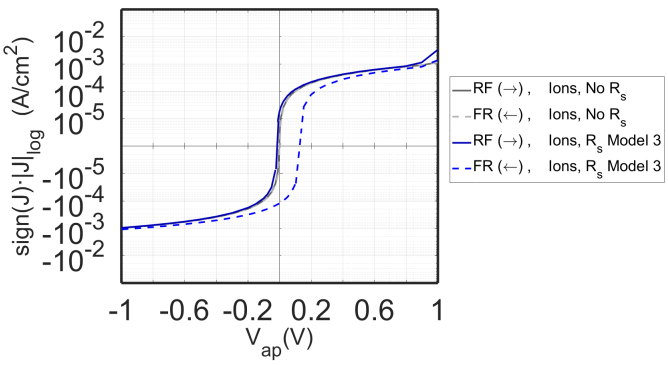

(a)

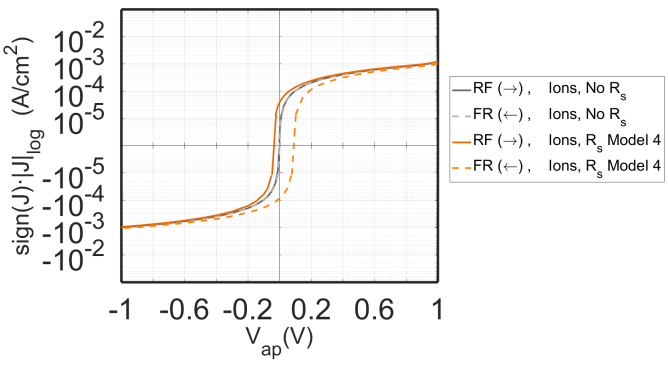

(b)

Figure 10: Fast $J-V$ curves in dark conditions calculated with $N_{ion} = 5\times10^{17}$ cm^{-3}, a shunt resistance $R_{shunt} = 10^3$ Ω·cm^2 and using (a) Model 3 with $B_S = 10^{-14} cm^3 s^{-1}$; and (b) Model 4 with $\tau_n = \tau_p = 1$ ms.

for Model 3, shows a change in the slope at high V_{ap}; this is explained by the fact that in this voltage range, the diode current J_{diode} surpasses the value of the leakage current J_{leak}. Figure S18 in SI shows the $J-V$ curve of Fig. 10a decomposed into J_{leak} and J_{diode}, confirming this fact.

5. Conclusions

This work reinforces the need to study $J-V$ curves of PSCs in dark conditions for better understanding of phenomena undetected under illumination. Our results highlight the importance of considering appropriate recombination model for the pvk/CTL interfaces in order to interpret the hysteresis observed at low voltages in $J-V$ curves measured in PSCs in dark conditions.

The best qualitative agreement between our simulations and the J-V curve experiments in dark conditions was obtained for models that include cross-recombination in an effective finite-thickness interface layer. This effective medium can be seen as a semiconductor buffer layer in which the perovskite is blended with the CTL, and it is characterized by an effective intrinsic carrier concentration $n_{i,eff}$ defined as the intrinsic carrier concentration of a semiconductor with effective energy band gap $Eg_{eff} = Ec,_{pvk} - Ev,_{HTL}$ for the HTL/pvk interface, and $Eg_{eff} = Ec,_{ETL} - Ev,_{pvk}$ for the pvk/ETL interface.

We have tested other cross-recombination models that succeed in reproducing hysteresis loops around $V_{ap} = 0$ V in $J-V$ curves in dark conditions. However, they fail to reproduce the zero value of the current density in equilibrium at $V_{ap} = 0$ V.

Several analyses were carried out considering the effects of (i) the interface recombination coefficient and interface trapping time constants, (ii) the thickness of the effective interface layer, (ii) the ion concentration, and (iii) the band alignment at the interfaces on the hysteresis loop of the $J-V$ curves in dark conditions. It was shown that the interface recombination must be suppressed in both interfaces for the hysteresis to be negligible. Importantly, hysteresis loop not only increase with mobile ion concentration, but also with the width of the buffer layer for interface recombination

Finally, the numerical reproduction of the large values of hysteretic transient open-circuit voltages are only found in our simulations with the inclusion of parasitic shunt resistance leakages.

References

[1] O. Almora, C. I. Cabrera, S. Erten-Ela, K. Forberich, K. Fukuda, F. Guo, J. Hauch, A. W. Y. Ho-Baillie, T. J. Jacobsson, R. A. J. Janssen, T. Kirchartz, M. A. Loi, X. Mathew, D. B. Mitzi, M. K. Nazeeruddin, U. W. Paetzold, B. P. Rand, U. Rau, T. Someya, E. Unger, L. Vaillant-Roca, C. J. Brabec, Device performance of emerging photovoltaic materials (version 4), Adv. Energy Mater. 14 (4) (2024) 2303173.

[2] S. De Wolf, J. Holovsky, S.-J. Moon, P. Löper, B. Niesen, M. Ledinsky, F.-J. Haug, J.-H. Yum, C. Ballif, Organometallic halide perovskites: Sharp optical absorption edge and its relation to photovoltaic performance, J. Phys. Chem. Lett. 5 (6) (2014) 1035–1039.

[3] S. G. Motti, D. Meggiolaro, S. Martani, R. Sorrentino, A. J. Barker, F. De Angelis, A. Petrozza, Defect activity in lead halide perovskites, Adv. Mater. 31 (47) (2019) 1901183.

[4] H. J. Snaith, Perovskites: The emergence of a new era for low-cost, high-efficiency solar cells, J. Phys. Chem. Lett. 4 (21) (2013) 3623–3630.

[5] NREL, Efficiency chart, https://www.nrel.gov/pv/cell-efficiency.html.

[6] M. A. Green, E. D. Dunlop, M. Yoshita, N. Kopidakis, K. Bothe, G. Siefer, D. Hinken, M. Rauer, J. Hohl-Ebinger, X. Hao, Solar cell efficiency tables (version 64), Prog. Photovoltaics: Research and Applications 32 (7) (2024) 425–441.

[7] D. Moia, J. Maier, Ion transport, defect chemistry, and the device physics of hybrid perovskite solar cells, ACS Energy Lett. 6 (4) (2021) 1566–1576.

[8] Y. Zhao, W. Zhou, Z. Han, D. Yu, Q. Zhao, Effects of ion migration and improvement strategies for the operational stability of perovskite solar cells, Phys. Chem. Chem. Phys. 23 (2021) 94–106.

[9] H. J. Snaith, A. Abate, J. M. Ball, G. E. Eperon, T. Leijtens, N. K. Noel, S. D. Stranks, J. T.-W. Wang, K. Wojciechowski, W. Zhang, Anomalous hysteresis in perovskite solar cells, J. Phys. Chem. Lett. 5 (9) (2014) 1511–1515.

[10] O. Almora, G. Garcia-Belmonte, Light capacitances in silicon and perovskite solar cells, Sol. Energy 189 (2019) 103–110.

[11] S. van Reenen, M. Kemerink, H. J. Snaith, Modeling anomalous hysteresis in perovskite solar cells, J. Phys. Chem. Lett. 6 (2015) 3808–3814.

[12] P. Calado, A. M. Telford, D. Bryant, X. Li, J. Nelson, B. C. O'Regan, P. R. F. Barnes, Evidence for ion migration in hybrid perovskite solar cells with minimal hysteresis, Nat. Commun. 7 (2016) 13831.

[13] S. E. J. O'Kane, G. Richardson, A. Pockett, R. G. Niemann, J. M. Cave, N. Sakai, G. E. Eperon, H. J. Snaith, J. M. Foster, P. J. Cameron, A. B. Walker, Measurement and modelling of dark current decay transients in perovskite solar cells, J. Mater. Chem. C 5 (2) (2017) 452–462.

[14] P. Lopez-Varo, J. A. Jiménez-Tejada, M. García-Rosell, J. A. Anta, S. Ravishankar, A. Bou, J. Bisquert, Effects of ion distributions on charge collection in perovskite solar cells, ACS Energy Lett. 2 (6) (2017) 1450–1453.

[15] T. S. Sherkar, C. Momblona, L. Gil-Escrig, J. Ávila, M. Sessolo, H. J. Bolink, L. J. A. Koster, Recombination in perovskite solar cells: Significance of grain boundaries, interface traps, and defect ions, ACS Energy Lett. 2 (5) (2017) 1214–1222.

[16] M. García-Rosell, A. Bou, J. A. Jiménez-Tejada, J. Bisquert, P. Lopez-Varo, Analysis of the influence of selective contact heterojunctions on the performance of perovskite solar cells, J. Phys. Chem. C 122 (25) (2018) 13920–13925.

[17] N. Tessler, Y. Vaynzof, Insights from device modeling of perovskite solar cells, ACS Energy Lett. 5 (4) (2020) 1260–1270.

[18] S. Kim, S. Bae, S.-W. Lee, K. Cho, K. D. Lee, H. Kim, S. Park, G. Kwon, S.-W. Ahn, H.-M. Lee, Y. Kang, H.-S. Lee, D. Kim, Relationship between ion migration and interfacial degradation of ch3nh3pbi3 perovskite solar cells under thermal conditions, Sci. Rep-UK 7 (1) (2017) 2045–2322.

[19] Y. Huang, P. Lopez-Varo, B. Geffroy, H. Lee, J.-E. Bourée, A. Mishra, P. Baranek, A. Rolland, L. Pedesseau, J.-M. Jancu, J. Even, J.-B. Puel, M. Gueunier-Farret, Detrimental effects of ion migration in the perovskite and hole transport layers on the efficiency of inverted perovskite solar cells, J. Photon. Energy 10 (2) (2020) 1 – 9.

[20] R. Gottesman, P. Lopez-Varo, L. Gouda, J. A. Jimenez-Tejada, J. Hu, S. Tirosh, A. Zaban, J. Bisquert, Dynamic phenomena at perovskite/electron-selective contact interface as interpreted from photovoltage decays, Chem 1 (5) (2016) 776 – 789.

[21] O. Almora, I. Zarazua, E. Mas-Marza, I. Mora-Sero, J. Bisquert, G. Garcia-Belmonte, Capacitive dark currents, hysteresis, and electrode polarization in lead halide perovskite solar cells, J. Phys. Chem. Lett. 6 (9) (2015) 1645–1652.

[22] M. T. Neukom, A. Schiller, S. Züfle, E. Knapp, J. Ávila, D. Pérez-del Rey, C. Dreessen, K. P. Zanoni, M. Sessolo, H. J. Bolink, B. Ruhstaller, Consistent device simulation model describing perovskite solar cells in steady-state, transient, and frequency domain, ACS Appl. Mater. Interfaces 11 (2019) 23320–23328.

[23] S. Bitton, N. Tessler, Perovskite ionics – elucidating degradation mechanisms in perovskite solar cells via device modelling and iodine chemistry, Energy Environ. Sci. 16 (2023) 2621–2628.

[24] T. Wang, B. Daiber, J. M. Frost, S. A. Mann, E. C. Garnett, A. Walsh, B. Ehrler, Indirect to direct bandgap transition in methylammonium lead halide perovskite, Energy Environ. Sci. 10 (2) (2017) 509–515.

[25] L. Wang, K. Wang, G. Xiao, Q. Zeng, B. Zou, Pressure-induced structural evolution and band gap shifts of organometal halide perovskite-based methylammonium lead chloride, J. Phys. Chem. Lett. 7 (24) (2016) 5273–5279.

[26] F. Ruf, P. Rietz, M. F. Aygüler, I. Kelz, P. Docampo, H. Kalt, M. Hetterich, The bandgap as a moving target: Reversible bandgap instabilities in multiple-cation mixed-halide perovskite solar cells, ACS Energy Lett. 3 (12) (2018) 2995–3001.

[27] M. I. Dar, G. Jacopin, S. Meloni, A. Mattoni, N. Arora, A. Boziki, S. M. Zakeeruddin, U. Rothlisberger, M. Grätzel, Origin of unusual bandgap shift and dual emission in organic-inorganic lead halide perovskites, Science Advances 2 (10).

[28] D. B. Straus, R. J. Cava, Tuning the band gap in the halide perovskite cspbbr3 through sr substitution, ACS Appl. Mater. Interfaces 14 (30) (2022) 34884–34890, pMID: 35867850.

[29] H. Zhang, Z. Bi, Z. Zhai, H. Gao, Y. Liu, M. Jin, M. Ye, X. Li, H. Liu, Y. Zhang, X. Li, H. Tan, Y. Xu, L. Yang, Revealing unusual bandgap shifts with temperature and bandgap renormalization effect in phase-stabilized metal halide perovskite thin films, Adv. Funct. Mater. 34 (9) (2024) 2302214.

[30] S. A. Kulkarni, T. Baikie, P. P. Boix, N. Yantara, N. Mathews, S. Mhaisalkar, Band-gap tuning of lead halide perovskites using a sequential deposition process, J. Mater. Chem. A 2 (2014) 9221–9225.

[31] J. Kim, S.-H. Lee, C.-H. Chung, K.-H. Hong, Systematic analysis of the unique band gap modulation of mixed halide perovskites, Phys. Chem. Chem. Phys. 18 (2016) 4423–4428.

[32] D. Meggiolaro, E. Mosconi, F. De Angelis, Formation of surface defects dominates ion migration in lead-halide perovskites, ACS Energy Lett. 4 (3) (2019) 779–785.

[33] Z. Li, C. Xiao, Y. Yang, S. P. Harvey, D. H. Kim, J. A. Christians, M. Yang, P. Schulz, S. U. Nanayakkara, C.-S. Jiang, J. M. Luther, J. J. Berry, M. C. Beard, M. M. Al-Jassim, K. Zhu, Extrinsic ion migration in perovskite solar cells, Energy Environ. Sci. 10 (5) (2017) 1234–1242.

[34] J. Diekmann, F. Peña-Camargo, N. Tokmoldin, J. Thiesbrummel, J. Warby, E. Gutierrez-Partida, S. Shah, D. Neher, M. Stolterfoht, Determination of mobile ion densities in halide perovskites via low-frequency capacitance and charge extraction techniques, J. Phys. Chem. Lett. 14 (18) (2023) 4200–4210.

[35] W. Shockley, W. T. Read, Statistics of the recombinations of holes and electrons, Phys. Rev. 87 (5) (1952) 835–842.

[36] R. N. Hall, Electron-hole recombination in germanium, Phys. Rev. 87 (2) (1952) 387–387.

[37] J. Wei, Q. Wang, J. Huo, F. Gao, Z. Gan, Q. Zhao, H. Li, Mechanisms and suppression of photoinduced degradation in perovskite solar cells, Adv. Energy Mater. 11 (3) (2021) 2002326.

[38] S. Svanström, T. J. Jacobsson, T. Sloboda, E. Giangrisostomi, R. Ovsyannikov, H. Rensmo, U. B. Cappel, Effect of halide ratio and cs+ addition on the photochemical stability of lead halide perovskites, J. Mater. Chem. A 6 (44) (2018) 22134–22144.

[39] O. Almora, Y. Zhao, X. Du, T. Heumueller, G. J. Matt, G. Garcia-Belmonte, C. J. Brabec, Light intensity modulated impedance spectroscopy (limis) in all-solid-state solar cells at open-circuit, Nano Energy 75 104982.

[40] K. Zheng, M. Abdellah, Q. Zhu, Q. Kong, G. Jennings, C. A. Kurtz, M. E. Messing, Y. Niu, D. J. Gosztola, M. J. Al-Marri, X. Zhang, T. Pullerits, S. E. Canton, Direct experimental evidence for photoinduced strong-coupling polarons in organolead halide perovskite nanoparticles, J. Phys. Chem. Lett. 7 (22) (2016) 4535–4539.

[41] Y. Kanemitsu, Trion dynamics in lead halide perovskite nanocrystals, J. Chem. Phys. 151 (17).

[42] K. Fan, C. C. S. Chan, L. Yuan, K. Yan, K. S. Wong, New insights into hot-charge relaxation in lead halide perovskite: Dynamical bandgap change, hot-biexciton effect, and photo-bleaching shift, ACS Photonics 9 (7) (2022) 2304–2314.

[43] B. Li, Y. Li, C. Zheng, D. Gao, W. Huang, Advancements in the stability of perovskite solar cells: degradation mechanisms and improvement approaches, RSC Advances 6 (44) (2016) 38079–38091.

[44] C. Zhao, B. Chen, X. Qiao, L. Luan, K. Lu, B. Hu, Revealing underlying processes involved in light soaking effects and hysteresis phenomena in perovskite solar cells, Adv. Energy Mater. 5 (14) (2015) 1500279.

[45] G. Garcia-Belmonte, J. Bisquert, Distinction between capacitive and noncapacitive hysteretic currents in operation and degradation of perovskite solar cells, ACS Energy Lett. 1 (4) (2016) 683–688.

[46] O. Almora, C. Aranda, I. Zarazua, A. Guerrero, G. Garcia-Belmonte, Noncapacitive hysteresis in perovskite solar cells at room temperature, ACS Energy Lett. 1 (1) (2016) 209–215.

[47] E. Hernández-Balaguera, B. Arredondo, G. d. Pozo, B. Romero, Exploring the impact of fractional-order capacitive behavior on the hysteresis effects of perovskite solar cells: A theoretical perspective, Commun. Non-

linear Sci. 90 (2020) 105371.
[48] E. Ghahremanirad, O. Almora, S. Suresh, A. A. Drew, T. H. Chowdhury, A. R. Uhl, Beyond protocols: Understanding the electrical behavior of perovskite solar cells by impedance spectroscopy, Adv. Energy Mater. 13 (30).
[49] Y. Zhang, M. Liu, G. E. Eperon, T. C. Leijtens, D. McMeekin, M. Saliba, W. Zhang, M. de Bastiani, A. Petrozza, L. M. Herz, M. B. Johnston, H. Lin, H. J. Snaith, Charge selective contacts, mobile ions and anomalous hysteresis in organic–inorganic perovskite solar cells, Mater. Horiz. 2 (3) (2015) 315–322.
[50] A. O. Álvarez, F. Lédée, M. García-Batlle, P. López-Varo, E. Gros-Daillon, J. Mayén Guillén, J.-M. Verilhac, T. Lemercier, J. Zaccaro, L. F. Marsal, G. Garcia-Belmonte, O. Almora, Ionic field screening in mapbbr3 crystals from remnant sensitivity in x-ray detection, ACS Phys. Chem. Au 3 (4) (2023) 386–393.
[51] O. Almora, D. Miravet, I. Gelmetti, G. Garcia-Belmonte, Long-term field screening by mobile ions in thick metal halide perovskites: Understanding saturation currents, Phys. Status Solidi RRL 16 (12) 202200336.
[52] A. O. Alvarez, M. García-Batlle, F. Lédée, E. Gros-Daillon, J. M. Guillén, J. Verilhac, T. Lemercier, J. Zaccaro, L. F. Marsal, O. Almora, G. Garcia-Belmonte, Ion migration and space-charge zones in metal halide perovskites through short-circuit transient current and numerical simulations, Adv. Electron. Mater.
[53] K. Majhi, L. Bertoluzzi, K. J. Rietwyk, A. Ginsburg, D. A. Keller, P. Lopez-Varo, A. Y. Anderson, J. Bisquert, A. Zaban, Combinatorial investigation and modelling of moo3 hole-selective contact in tio2|co3o4|moo3 all-oxide solar cells, Adv. Mater. Interfaces 3 (1) (2016) 1500405.
[54] N. Courtier, J. Cave, A. B. Walker, G. Richardson, J. M. Foster, Ionmonger: a free and fast planar perovskite solar cell simulator with coupled ion vacancy and charge carrier dynamics, J. Comput. Electron. 18 (2019) 1435–1449.
[55] P. Lopez-Varo, J. A. Jiménez-Tejada, M. García-Rosell, S. Ravishankar, G. Garcia-Belmonte, J. Bisquert, O. Almora, Device physics of hybrid perovskite solar cells: Theory and experiment, Adv. Energy Mater. 8 (14) (2018) 1702772.
[56] P. Lopez-Varo, J. A. Jiménez-Tejada, M. García-Rosell, J. A. Anta, S. Ravishankar, A. Bou, J. Bisquert, Effects of ion distributions on charge collection in perovskite solar cells, ACS Energy Lett. 2 (6) (2017) 1450–1453.
[57] O. Almora, P. Lopez-Varo, K. T. Cho, S. Aghazada, W. Meng, Y. Hou, C. Echeverría-Arrondo, I. Zimmermann, G. J. Matt, J. A. Jiménez-Tejada, C. J. Brabec, M. K. Nazeeruddin, G. Garcia-Belmonte, Ionic dipolar switching hinders charge collection in perovskite solar cells with normal and inverted hysteresis, Sol. Energy Mater. Sol. Cells 195 (2019) 291–298.
[58] P. Calado, I. Gelmetti, B. Hilton, M. Azzouzi, J. Nelson, P. R. F. Barnes, Driftfusion: an open source code for simulating ordered semiconductor devices with mixed ionic-electronic conducting materials in one dimension, J. Comput. Electron. 21 (4) (2022) 960–991.
[59] P. Calado, I. Gelmetti, B. Hilton, M. Azzouzi, J. Nelson, P. R. F. Barnes, Correction to: Driftfusion: an open source code for simulating ordered semiconductor devices with mixed ionic-electronic conducting materials in one dimension, J. Comput. Electron. 21 (5) (2022) 1189–1189.
[60] X. Zhang, J.-X. Shen, W. Wang, C. G. V. de Walle, First-principles analysis of radiative recombination in lead-halide perovskites, ACS Energy Lett. 3 (10) (2018) 2329–2334.
[61] P. Langevin, Recombinaison et mobilites des ions dans les gaz., Ann. Chim. Phys 28 (1903) 433–530.
[62] L. M. Herz, Charge-carrier mobilities in metal halide perovskites: Fundamental mechanisms and limits, ACS Energy Lett. 2 (7) (2017) 1539–1548.
[63] L. F. Schneemeyer, R. B. van Dover, R. M. Fleming, High dielectric constant Hf–Sn–Ti–O thin films, Appl. Phys. Lett. 75 (13) (1999) 1967–1969.
[64] J. Thiesbrummel, S. Shah, E. Gutierrez-Partida, F. Zu, F. Peña-Camargo, S. Zeiske, J. Diekmann, F. Ye, K. P. Peters, K. O. Brinkmann, P. Caprioglio, A. Dasgupta, S. Seo, F. A. Adeleye, J. Warby, Q. Jeangros, F. Lang, S. Zhang, S. Albrecht, T. Riedl, A. Armin, D. Neher, N. Koch, Y. Wu, V. M. Le Corre, H. Snaith, M. Stolterfoht, Ion-induced field screening as a dominant factor in perovskite solar cell operational stability, Nat. Energy 9 (6) (2024) 664–676.
[65] O. Almora, P. López-Varo, R. Escalante, J. Mohanraj, L. F. Marsal, S. Olthof, J. A. Anta, Degradation analysis of perovskite solar cells via short-circuit impedance spectroscopy: A case study on niox passivation (2024).